Sensors and Materials, Vol. 34, No. 6 (2022) 2089–2104
MYU Tokyo

S & M 2958

Smartphone-based On-chip Homogenous Sensing by Analysis of Dynamics of Oscillating Polystyrene Particles under Dielectrophoretic Forces

Jaiyam Sharma, Taisuke Ono, Naohito Satake, and Adarsh Sandhu*

Graduate School of Information and Engineering, University of Electro-Communications,
1-5-1 Chofugaoka, Chofu, Tokyo 182-8585, Japan

(Received February 28, 2022; accepted May 6, 2022)

Keywords: biosensing, medical diagnostics, point-of-care testing, functionalized particles

Compact, rapid, and inexpensive smartphone-based point-of-care diagnostics is developing rapidly to replace conventional medical diagnostic procedures that necessitate specialized skills and bulky instruments. Smartphone-based biosensing protocols proposed to date involve "heterogenous" interactions of labels with functionalized sensing surfaces. In contrast, "homogenous" protocols do not require surface functionalization but are bulky and unsuitable for point-of-care diagnostics. In this work, we demonstrate a smartphone-based homogenous biosensing protocol that is portable, rapid, and low cost. Currents passed through microelectrode patterns fabricated onto silicon substrates produced dielectrophoretic forces that induced harmonic oscillations of 1-μm-diameter carboxyl-coated polystyrene particles suspended in aqueous solutions at well-defined heights above the surfaces of the chips. Next, we introduced 200-nm-diameter polystyrene particles functionalized with complementary amine compounds into the solution, which interacted with the larger particles, thereby significantly changing the oscillation dynamics of the larger beads. A smartphone was used to record the motion of the beads. Particle tracking and filtering algorithms were used to extract information about the oscillation of the particles and detect changes in their dynamics. The results showed that our approach enables the detection of the concentration of aminated particles with a smartphone within 1 min without requiring any prior functionalization of the biochip.

1. Introduction

Smartphone-based point-of-care diagnostics has developed rapidly in the last decade[1,2] with the goal of replacing conventional medical diagnostic technologies, which are time-consuming, bulky, and expensive, limiting their applications in remote locations and public health emergencies. However, most diagnostic protocols based on smartphones developed to date involve the complementary interaction between targets and labels with a solid sensing surface in a so-called heterogenous interaction. The heterogenous approach requires the preparation of high-quality sensing surfaces with selectively immobilized probes. This has two disadvantages.

*Corresponding author: e-mail: sandhu@uec.ac.jp
https://doi.org/10.18494/SAM3881

ISSN 0914-4935
https://myukk.org/

First, sensors with solid sensing surfaces often require numerous[3,4] and expensive microfabrication steps. Second, the heterogenous approach leads to nonspecific interactions[5] of the biological labels with the sensing surface in addition to the sensor noise and environmental noise inherent to the measurement setup. These factors limit the practical applications of heterogenous biosensors for smartphone-based point-of-care testing.

The limitations of heterogenous biosensing approaches have accelerated the development of protocols that do not require a solid sensing surface and where the biochemical reaction between the target and probe molecules occurs completely within a homogenous liquid medium.[6,7] These "homogenous" biosensing protocols offer significant advantages such as low nonspecific interactions and simpler sample preparation because sensing surfaces do not require functionalizion with probe molecules. However, most homogenous protocols demonstrated to date are not portable and require a bulky experimental setup, making them unsuitable for integration with smartphones. Park *et al.*[7] demonstrated the quantitative detection of avidin by measurement of the optical transmission from chains of magnetic particles in a homogenous medium under a rotating magnetic field. The magnetic field was rotated by sinusoidally varying the currents in a pair of large Helmholtz coils, which makes this method too bulky for point-of-care diagnostics. DuVall *et al.*[8] demonstrated the detection of the *C. difficile* pathogen based on magnetic bead aggregation in a homogenous medium under a rotating magnetic field. Although the analysis of magnetic particle aggregation in their study was performed on a smartphone, their experimental setup required four industrial stepper motors, long steel guiding rails, and a large power supply, making the protocol generally unsuitable for portable diagnostics.

Here, we propose a portable and rapid smartphone-based homogenous biosensing protocol utilizing polystyrene particles, sometimes referred to as "polystyrene beads", as labels to address the limitations of the previous approaches[6,7] discussed above. Specifically, our method involves:

(a) inducing specific interactions between polystyrene particles moving freely in a homogenous medium using horizontal on-chip dielectrophoretic forces,
(b) recording high-resolution videos of thousands of polystyrene particles during the biochemical reaction, and
(c) analyzing the motion of every particle in the video with submicron resolution to identify which particles have interacted specifically with the target molecules of interest.

Experimental results on a simple carboxyl–amine ($COOH–NH_2$) model system showed that homogenous chemical interactions can be detected with the proposed approach using on-chip forces within 1 min and that the quantitative detection of amine targets can be achieved. We obtain a limit of detection of 50 μg/ml for NH_2. The results from this research demonstrate that our method is promising for realizing innovative smartphone-based point-of-care diagnostics.

Magnetic-particle-based homogenous biosensing protocols proposed to date have focused on having a large 3D volume of the sample under analysis and obtaining a signal from the whole volume. Although analyzing a large volume has inherent advantages such as low statistical noise margins, producing uniform mixing forces throughout the volume requires large and bulky equipment as discussed above. In contrast, heterogenous biosensing methods are able to produce "on-chip" electromagnetic forces in a small region above the sensing surface, thereby resulting

in small, portable systems and high reproducibility of the forces. A quantitative analysis of the forces on magnetic particles suspended in a liquid medium over a solid substrate[9] showed that the various vertical forces acting on the particles cancel out, resulting in the particles being suspended at an equilibrium height above the substrate, as shown in Fig. 1.

This poses a challenge for heterogenous methods, especially those employing magnetic sensors. High-gradient vertical magnetic fields are required to bring the particles close to the sensing surface because the sensor output strongly depends on the distance of the particle from the surface.[10,11]

In contrast to heterogenous methods, we utilize this property to our advantage by noting that if horizontal forces are applied to functionalized particles suspended at an equilibrium height above the substrate, homogenous interactions of polystyrene particles with complementary targets can be achieved using only on-chip forces, thereby enabling the development of a portable homogenous system. A constant equilibrium height of the particles from the substrate results in the particles lying on a plane, which can be imaged via a smartphone. We use this property to obtain measurements from a thin plane rather than from the entire volume as in previous homogenous approaches. As we discuss in Sect. 2.8, this limitation of the proposed method is compensated for by its provision of much more specific details about the motion of each particle under observation, rather than providing gross statistical estimates from a volume as in previous approaches[6,7]. Therefore, this method can in principle achieve very low limits of detection down to the interaction of a single polystyrene particle with complementary targets.

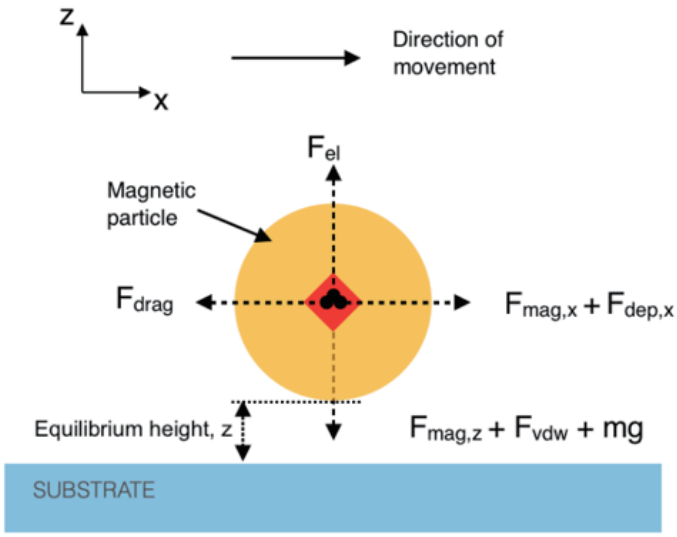

Fig. 1. (Color online) Free-body diagram of a magnetic particle suspended in a liquid medium over a substrate (adapted from Ref. 9).

2. Methods

2.1 Proposed protocol

A schematic of the proposed approach is shown in Fig. 2. The method involves two types of functionalized polystyrene particles: large 1-μm-diameter particles whose surface was terminated with a carboxyl group and small 200-nm-diameter particles whose surface was terminated with the complementary amine group. The particles were prepared separately and introduced one after another in a reaction well on an actuator consisting of four linear electrodes: AB, CD, PQ, and RS. The extent of the reaction well is not shown in Fig. 2, but can be seen in Fig. 3 as discussed later. Points B and C were electrically connected via an external jumper, and points Q and R were similarly connected. After the particles were introduced, sinusoidal currents were applied to the electrodes. Current $I_x = I_0 \sin(\omega t)$ was applied across electrodes AB and CD and current $I_y = I_0 \cos(\omega t)$ was applied to electrodes PQ and RS, as shown in the top view of Fig. 2. As shown in the side view of Fig. 2(a), the flow of currents induced harmonic oscillations of the polystyrene particles due to dielectrophoretic forces (see Sect. 2.2). The harmonic oscillations caused the two types of solutions containing particles with complementary surfaces to mix and interact with each other. As a result, the amplitude of motion of the particles changed when specific interactions occurred, as shown in Fig. 2(b). During the application of the

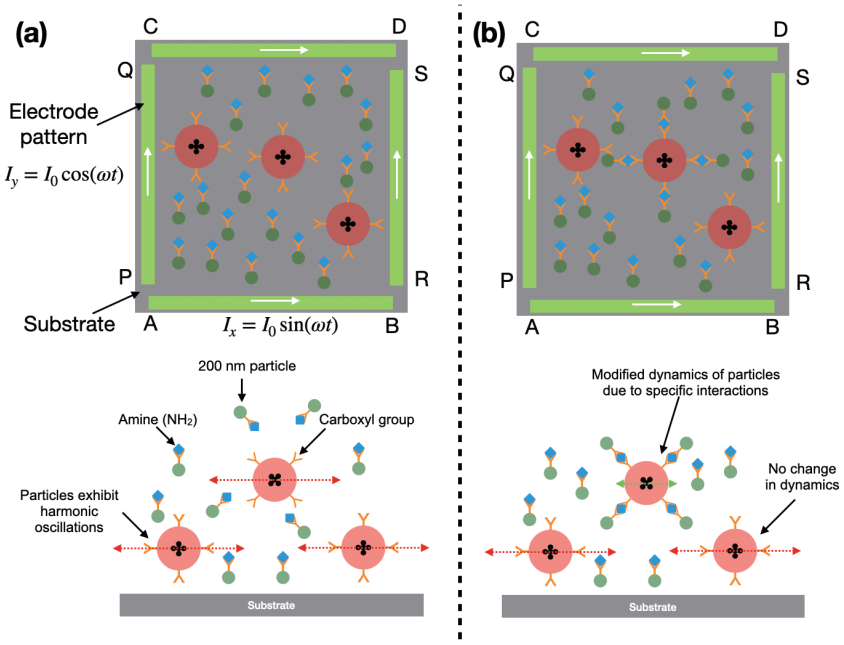

Fig. 2. (Color online) Schematic of the proposed homogenous sensing protocol. Orange crosses represent chemical interactions between carboxyl and amine groups. (a) The application of currents causes harmonic oscillations in magnetic particles, whose amplitude depends on the interaction between the particles. (b) When particles interact with each other, the amplitude of motion changes. Although the particles lie on a horizontal plane, as discussed above, they are shown staggered in the side views for ease of illustration. The actuator also contains connector pads, which are not shown in this illustration.

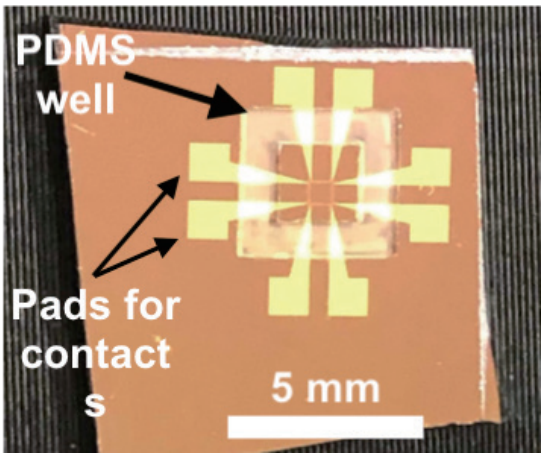

Fig. 3. (Color online) Photograph of the fabricated actuator with the reaction well installed.

currents and the biochemical reaction, the particle plane was imaged with a smartphone-based microscope and a high-resolution video was recorded. The particle dynamics were analyzed via optical tracking and the changes in the amplitude of oscillations of the particles with respect to a control sample were quantified. The extent of the changes in the amplitude allows quantitative detection of the target.

2.2 Dielectrophoretic forces and design of the actuator

Previous biosensing approaches, especially heterogenous ones, have relied on the application of magnetic forces to enable the manipulation of magnetic particles across and above the sensing surface. From basic electromagnetic theory, it is well known[12,13] that the amplitudes of electric and magnetic fields of a plane wave traveling in free space satisfy the relation $\left|\vec{E}\right|/\left|\vec{B}\right| = c$, where c is the speed of light in vacuum. Therefore, the amplitude of the electric field is several orders of magnitude greater than that of the magnetic field. The magnetic force acting on a particle suspended in a nonmagnetic medium ($\chi_m \approx 0$) is given by[9,14]

$$\overrightarrow{F_m} = \frac{V\chi_p}{\mu_0}\vec{B}\cdot\nabla\vec{B}, \tag{1}$$

where V is the volume of the particle, χ_p is its magnetic susceptibility, μ_0 is the permeability of vacuum, and $\vec{B}$ is the external magnetic field. The dielectrophoretic (DEP) force on a particle of a dielectric material placed in an inhomogenous external electric field $\vec{E}$ arises from the formation of induced dipoles in the dielectric and is given by[15]

$$\overrightarrow{F_{DEP}} = \frac{3V\varepsilon(\omega)}{2}\vec{E}\cdot\nabla\vec{E}, \tag{2}$$

where V is the volume of the particle and $\varepsilon(\omega)$ is the Clausius–Mossotti factor at the frequency ω of the applied field, given by $\varepsilon(\omega) = \frac{\varepsilon_m^* - \varepsilon_p^*}{\varepsilon_m^* + 2\varepsilon_p^*}$, where ε_p is the relative permittivity of the particle and ε_m is the relative permittivity of the surrounding medium. Typically, a biological medium such as water has negligible magnetic susceptibility ($\chi_m \approx -10^{-5}$) but a large relative permittivity ($\varepsilon_m \approx 80$). Magnetic particles are composed of iron oxide nanoparticle cores, which impart them with magnetic susceptibility of χ_p = 1–3 depending on the type of magnetism (superparamagnetic or ferromagnetic) and the size of the particle. The polymer material, typically polystyrene, composing the particles has a relative permittivity of ε_p = 2.4–2.7. Thus, from the above discussion, we conclude that the DEP forces on polystyrene particles are much greater than the magnetic forces. Therefore, the DEP forces produced by a current line actuator extend to much greater distances than the magnetic forces.

Previously, we demonstrated a current line actuator optimized for the application of high-gradient magnetic forces.[16] However, for currents of 20 mA, the magnetic field extends only to a maximum distance of ≈8–10 μm from the current line. In contrast, DEP forces allow us to increase the extent of the field by approximately two orders of magnitude at a given current. Thus, we made the following design decisions:

(a) The distance between AB and CD (as well as between PQ and RS) was 550 μm.
(b) The width of the current lines was 10 μm and the thickness of the electrode film was 200 nm.
(c) The amplitude I_0 of the applied sinusoidal current was 30 mA (RMS 21 mA) and the frequency was ω = 0.5 Hz.

These design parameters were selected to achieve acceptable DEP forces over large distances while reducing Joule heating and the number of steps required to fabricate the actuator. For example, most heterogenous sensors require a passivation layer to shield the biological fluid from the Joule heating of the underlying sensors, which would denature the proteins and prevent biological interactions. However, our design contains a simple current line actuator, and the low Joule heating eliminates the need for a passivation layer, resulting in a simpler fabrication process than that of magnetoresistive sensors integrated with actuators.[17] When sinusoidal currents are applied, DEP forces dominate over a large surface area and produce harmonic oscillations, whereas magnetic forces dominate close to the electrodes and induce anharmonic motion of the particles close to the electrodes.

2.3 Fabrication of the actuator

The actuator consists of a silicon nitride substrate with four linear current lines as described in Sect. 2.2. The substrate was coated with AZ5214E photoresist and the current line pattern was created using conventional photolithography. After development, a single electron beam deposition step was performed to deposit films of titanium (100 nm thickness) followed by gold (100 nm thickness). Lift-off was carried out to remove excess photoresist. As a result, only the electrode pattern remained on the substrate. Notably, no passivation layer was deposited. Finally, the prepared substrate was cleaned with acetone and ethanol and treated under oxygen plasma for 1 min to facilitate the installation of a reaction well fabricated from polydimethylsiloxane

(PDMS). Uniformly sized reaction wells were cut with a laser cutter to ensure that a constant volume of 3 μL was under analysis. The completed assembly is shown in Fig. 3.

2.4 Preparation of magnetic particles

As stated in Sect. 2.2, two types of polystyrene particles of different sizes were used. The large polystyrene particles (Dynabeads, Thermo Fisher Inc.) were 1 μm in diameter and the smaller particles were 200 nm in diameter (FG beads, Tamagawa Seiki Co. Ltd.). Both the 1-μm- and 200-nm-diameter particles contained iron oxide nanoparticles giving both types superparamagnetic properties, whereby the particles become magnetized and align along the directions of external magnetic fields, but disperse in aqueous solutions exhibiting random Brownian motion without external magnetic fields. The behavior of the particles described in this paper only rely on the dielectric properties of the particles, that is the action of electric fields on the polystyrene particles. The particle behavior is not due to magnetic effects. The reason we used these particles is because we have a wide selection of such particles from our legacy of 20 years or so of research on medical diagnostics using superparamagnetic particles. We wanted to see if the same particles—that we are able to functionalize and whose physical properties we are very familiar with—could be used for biosensing based on their dielectric properties.

The surfaces of the Dynabeads were terminated with carboxyl (COOH), whereas those of the FG beads were terminated with amine (NH_2). The particles were used as received from the manufacturer without surface modification. The Dynabeads were diluted to 2% by volume in a solution of deionized water and the FG beads were diluted with deionized water to five different concentrations: 100, 200, 240, 300, and 400 μg/mL. In addition, a solution of pure deionized water was prepared with no amine-functionalized particles as a control. During the experiment, a solution containing 1.5 μL of the amine-coated particles was first introduced into the reaction well, followed by a solution of 1.5 μL of the carboxyl-coated particles. Thus, the concentrations of amine in the final solutions were half of the initial concentrations, i.e., 50, 100, 120, 150, and 200 μg/mL.

2.5 Circuit design for application of currents

A printed circuit board (PCB) was designed to allow the rapid formation of contacts for the application of current. A chip holder was designed using CAD software and 3D-printed using a commercial FDM printer. The final completed assembly of the chip holder and PCB is shown in Fig. 4.

2.6 Optical assembly and application of current

The actuator and chip holder assembly was placed under a microscope (Olympus BX51). Although the microscope has an in-built camera, we utilized only the lens (20×, 0.4 NA) and the focusing apparatus of the microscope and not the camera. A smartphone was mounted on the eyepiece of the microscope and the substrate was imaged without using any advanced imaging

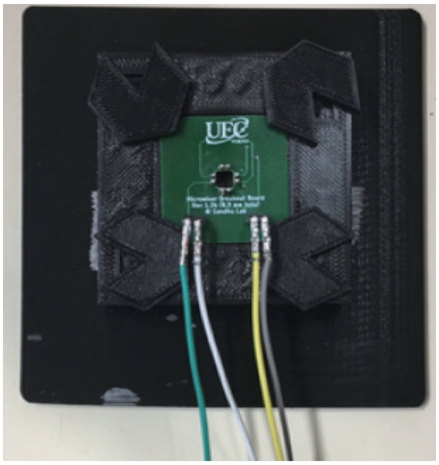

Fig. 4. (Color online) Photograph of the PCB and chip holder assembly. The actuator chip is underneath the PCB, below the hole milled out in the middle.

or color correction functionality of the microscope camera, as shown in Fig. 5. Although a low-cost microscope would have been more suitable for fully demonstrating the potential of our approach for point-of-care diagnostics, we note that a large number of low-cost, high-magnification, smartphone-based microscopes have been demonstrated in the literature.[18–21] Thus, we leave the development of a smartphone-based microscope as future work.

Similarly, a low-cost circuit can be developed for the application of sinusoidal currents. However, we used a commercial function generator (NF WF1974) in the experiments discussed here. The power consumed by the actuator was 0.126 W with a peak voltage of ±4.2 V and frequency of 0.5 Hz. Therefore, a low-cost circuit can be designed because no amplifiers, frequency synthesizers, or cooling equipment is necessary at such a low power and frequency. As with the optical setup, we leave this for future work.

The smartphone (iPhone 8, Apple Inc.) was used to record a 4K video (2160 × 3840 pixels) of the substrate at 24 fps. The recording was started at the time that the application of current was initiated. A video of just over 1 min (63–65 s) was recorded and a 10 s clip from 50 to 60 s was analyzed. After 1 min, the currents and video recording are halted. The recorded video was transferred wirelessly via a local SMB server connection to a PC for analysis.

2.7 Analysis of particle dynamics

Extracting biologically relevant information about the dynamics of particles from a video is a challenging problem. To summarize the challenges discussed in our previous work,[22] most particle tracking algorithms and software developed to date were developed for the study of cellular biology. Therefore, they focus on accurately tracking a single or a few fluorescent tags, which can be easily distinguished by their color, in stacks of a few images. Moreover, natural cells have very simple dynamics, such as Brownian or linear motion, which are explicitly incorporated into the tracking software. We developed an alternative particle tracking software, which can track tens of thousands of particles simultaneously and does not require any

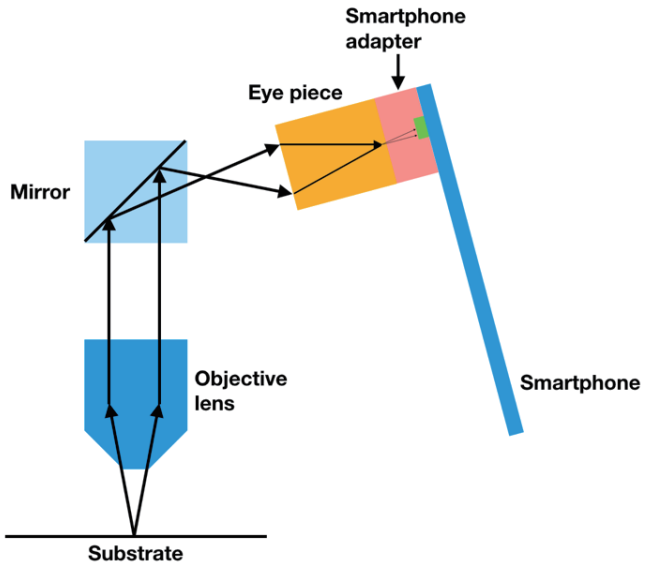

Fig. 5. (Color online) Schematic of the optical setup.

assumptions about the statistics of the motion of individual particles. This software is available as an open-source platform with a graphical interface[23] that can be freely used without requiring any knowledge of programming or the algorithms.

In this work, we build upon the capabilities of this software to extract information relevant to homogenous biosensing. As discussed in Sect. 2.3, DEP forces produce harmonic oscillations, whereas magnetic forces produce anharmonic motion. Thus, the trajectory of a particle is a combination of many types of motion. This makes it necessary to filter out the effect of particles that do not show harmonic oscillations as well as anharmonic effects in the trajectories of harmonically oscillating particles. Consider the set S of all particle trajectories along the x and y axes obtained by optical tracking, i.e.,

$$S = \left\{ \left(x_{i,t}, y_{i,t} \right) : 0 \le i \le N, \;\; 1 \le t \le 240 \right\}, \tag{3}$$

where i represents the particle number, N is the total number of particles in the field of view, and t represents the discrete time step represented as the frame number of the video being analyzed. Since the video is recorded at 24 fps and a 10 s clip is analyzed, the maximum value of t is 240. We perform the following steps to extract the amplitude of oscillations of particles, which are illustrated on experimental data in Fig. 6:

(a) A single-sided discrete Fourier transform (DFT) of the particle trajectories is performed for both the x- and y-trajectories. The power spectrum $PS\left(S(i,x)\right) = \left| DFT(x_{i,1:240}) \right|$ (and similarly for y) obtained by the DFT shows a peak at the frequency of the applied field (ω = 0.5 Hz) if the particle is oscillating. This peak is detected in an automated way by performing linear regression on the normalized log-log plot of the power spectrum, as shown in Fig. 6(b). The random sample consensus (RANSAC) algorithm is used while performing linear regression to avoid outliers resulting from the peak at ω = 0.5 Hz and noise at high frequencies. Note

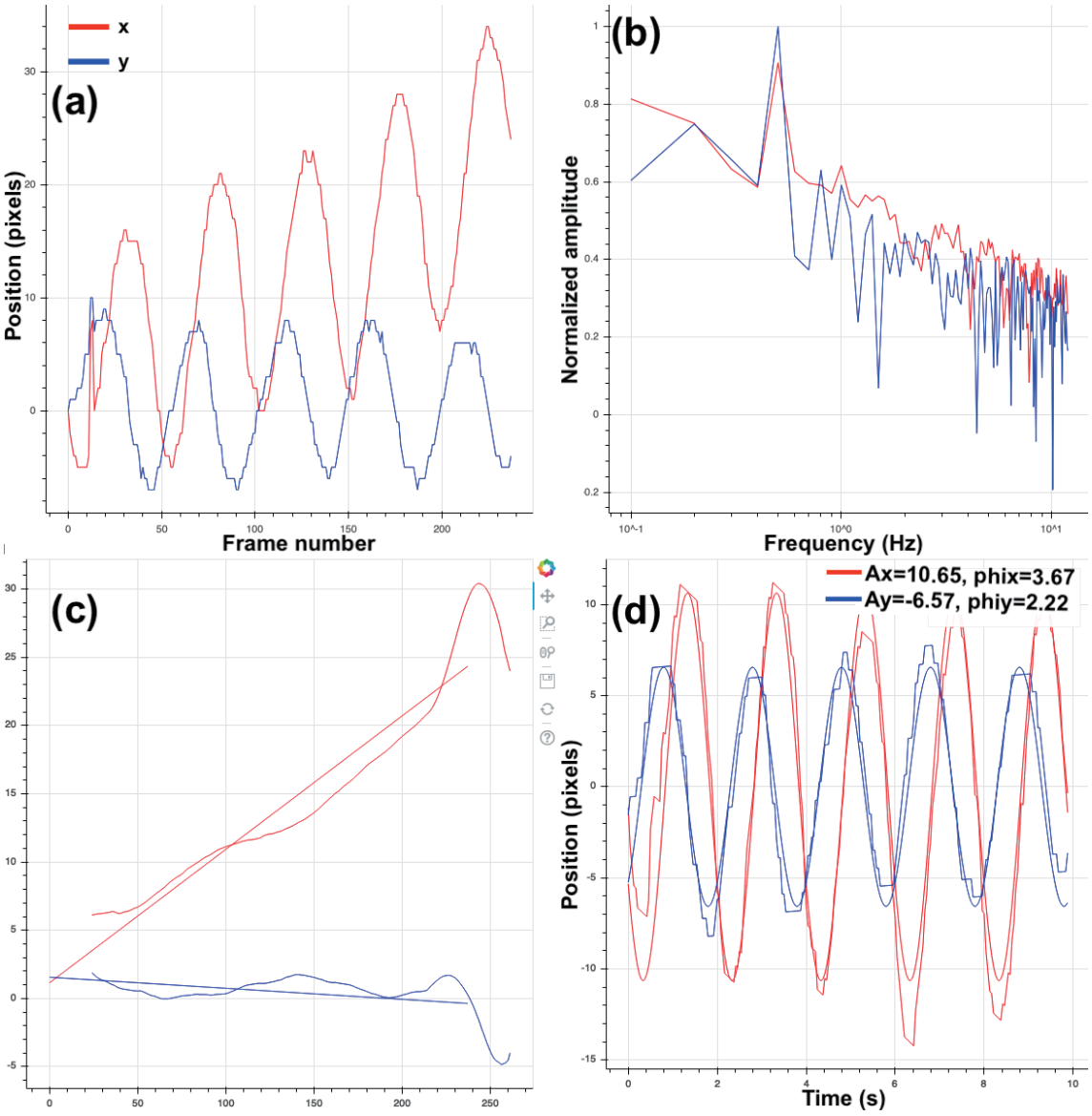

Fig. 6. (Color online) Processing steps described in Sect. 2.8. In all parts, red curves correspond to the x axis and blue curves correspond to the y axis. (a) Raw trajectory of a particle obtained by tracking. Drift in the trajectory superimposed on harmonic oscillations can be observed, (b) Single-sided DFT power spectrum for the trajectory shown in (a). The peaks observed for the x and y axes at 0.5 Hz are above the linear regression model of the power spectrum (not shown) by the threshold; thus, this particle is deemed to exhibit harmonic oscillations. (c) Drifts along the axes estimated by applying a moving average filter and fitting a linear regression model (using RANSAC) to the resulting curves. (d) Original trajectory detrended using the estimated linear drift model along each axis, where curve fitting is used to estimate the amplitude of motion of the particle along the two axes.

that since the sampling rate of our measurements is 24 Hz, by the Nyquist theorem, the maximum frequency in the single-sided DFT is 12 Hz. If the power spectrum at $\omega = 0.5$ Hz is higher than the linear regression value by a given threshold $T = 0.2$, the particle is considered to be oscillating. Thus, the set O of indices of the oscillating particles is given by

$$O = \left\{ i : PS\left(S(i,j)\right) > LR\left(S(i,j),\omega\right) + T, j \in (x,y) \right\}, \tag{4}$$

where $LR\left(S\left(i,j\right),\omega\right)$ represents the expected value of the power spectrum at the applied frequency ω obtained by the RANSAC linear regression model in the absence of harmonic oscillations.

(b) Once the oscillating particles have been identified, a sinusoidal curve can be fitted to the trajectories to find the amplitude of oscillation, but an additional step is necessary to reduce anharmonic motion in the particle trajectory before curve fitting. The trajectories of oscillating particles may drift over time due to the nonuniform nature of the fields. Thus, detrending of the drift is necessary. A median filter m_l (of kernel size l = 5) is applied to the trajectory, and subsequently, a moving average filter μ_w with a window size of one period of oscillation ($w = fps/\omega$ = 48) is applied to the trajectory, i.e.,

$$M(i,j) = \left\{ \mu_w\left(m_l\left(S(i,j)\right)\right) : i \in O, j \in (x,y) \right\}. \tag{5}$$

The filtered trends M are further filtered by fitting a linear regression model LR (with RANSAC) to reduce the deviations at the beginning and end of the time series data due to the moving average filter. This is shown in Fig. 6(c). The linear regression model is used to detrend the trajectories as follows:

$$D(i,j) = \left\{ S(i,j) - LR\left(M(i,j)\right) :\ i \in O,\ \ j \in (x,y) \right\}, \tag{6}$$

(c) The amplitude of motion $A_{i,j}$ and the phase $\phi_{i,j}$ of oscillating particle i along the j axis are estimated by fitting a sinusoidal motion model $C_{i,j}$ to the detrended trajectory data, as shown in Fig. 6(d), where

$$C_{i,j} = A_{i,j}\sin(\omega t + \phi_{i,j}) \quad \forall i \in O,\ \ \forall j \in (x,y), \tag{7}$$

(d) Next, we note that some particles are subjected to both DEP forces and magnetic forces. The amplitude of oscillations of these particles can be markedly different from those of the majority of particles and they can thus skew the statistics of motion of the particle population. Thus, the resulting amplitudes obtained by curve fitting are further filtered to reduce the effect of such particles. The average μ_{A_j} and standard deviation σ_{A_j} of the amplitudes are calculated for both the x and y axes ($j \in (x,y)$), and the particles whose amplitude differs from the average by more than one standard deviation are rejected. The resulting low-noise amplitudes are thus given by

$$L = \left\{ A_{k,j} : \left| A_{k,j} - \mu_{A_j} \right| \le \sigma_{A_j} \quad \forall j \in (x,y),\ \ k \in O \right\}, \tag{8}$$

(e) A histogram of the low-noise amplitudes L obtained after the above four steps is plotted and the mode of the histogram, i.e., the amplitude with the highest probability, is considered as

the amplitude of motion of the particles. As is clear from the above discussion, two oscillation amplitudes are obtained, one each for the x and y axes. These two amplitudes serve as a self-consistent metric for our method. The two amplitudes should be within the measurement resolution of one pixel, and a large difference between the two may indicate an experimental error. In our experimental results, the x and y amplitudes were always found to be within this limit, thereby passing this self-consistency test.

3. Results

Supplementary video V1 shows the trajectory of particles obtained by tracking on an experimentally obtained video. Here, we demonstrate the effectiveness of the processing described in Sect. 2.8. The red/yellow trajectory paths denote particles that are identified to exhibit harmonic oscillations (set O in Sect. 2.8), whereas the green paths denote particles that do not show harmonic oscillations. Here, the oscillation recognition step [step (a)] is run for each frame, i.e., the DFT calculations, power spectrum analysis, and RANSAC curve fitting are performed at each time step for each particle. Our efficient implementation of these routines allows us to perform the advanced analysis of particle trajectories and extract biologically relevant information from the raw video. The results show that the algorithm can recognize oscillating particles even with limited data (a few frames).

We now explain the results obtained with carboxyl-functionalized particles with various amounts of amine-functionalized particles. The amplitude of harmonic oscillations of 1-μm-diameter carboxyl-functionalized particles decreases with increasing concentration of amine particles in the solution. Since there is no external vertical electric or magnetic field and the surface of the substrate is not functionalized in any of our experiments, we conclude that the decrease in the oscillations is due to the increased mass of the chemically bonded beads in the homogenous suspension. The harmonic oscillations induced in carboxyl-functionalized particles enhance their probability of interacting with a complementary nanoparticle.

Supplementary video V2 shows a side-by-side comparison of the oscillations induced in the carboxyl-functionalized particles (without NH_2) when 200 μg/mL of amine-functionalized nanoparticles are present in the solution. The left panel (only COOH particles) shows that the particles have a large amplitude of motion, whereas the right panel shows that the oscillations are much less pronounced when complementary particles are present in the solution. A small part of the total sensing area is shown in the video for clarity of illustration because a collage of two full-resolution 4K video streams cannot be viewed on most displays without significant down-sampling. Figure 7 shows a comparison of the trajectories of one particle selected randomly from the two panels. It is clear from these results that the oscillations of 1-μm-diameter carboxyl particles are significantly reduced in the presence of amine-functionalized nanoparticles.

Figure 8 shows normalized histograms of particle oscillation amplitude in the x direction for various concentrations of amine-coated particles. The x axis represents the oscillation amplitude (in μm), whereas the vertical axis represents the probability of a given amplitude. The area under each curve is 1. The mode of the oscillation amplitude, i.e., the peak of the histogram, shifts to the left (decreases) as the concentration of amine-functionalized particles is increased. Thus, the

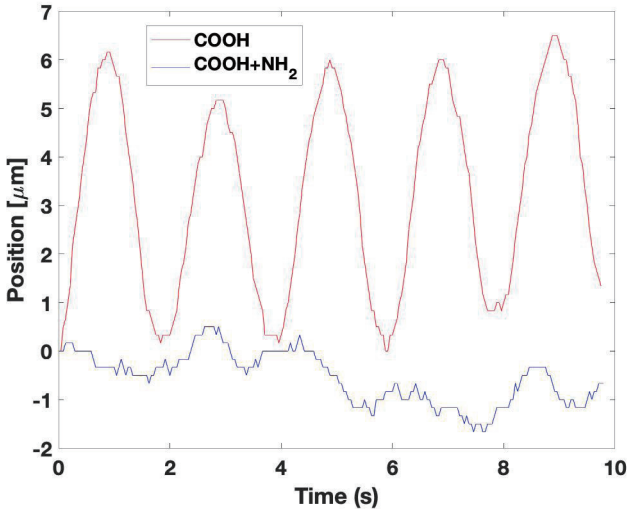

Fig. 7. (Color online) Comparison of the trajectories of two randomly selected particles, one from the left panel and the other from the right panel, in supplementary video V2.

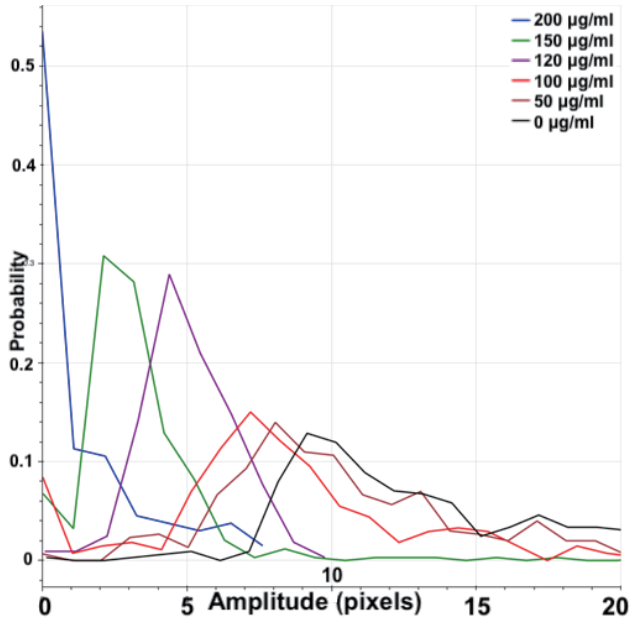

Fig. 8. (Color online) Histograms of particle oscillation amplitudes in x direction for various concentrations of amine-functionalized particles. Carboxyl particles (without NH_2) have the highest oscillation amplitude, which decreases as amine-functionalized particles are added.

peak position of the histogram is negatively correlated with the concentration of amine particles in solution.

Figure 9 shows a plot of the peak position for various concentrations of amine particles for both the x and y axes. We observe that both the x and y peak positions show excellent agreement and are within ±1 pixel of each other. The average amplitude decreases with increasing

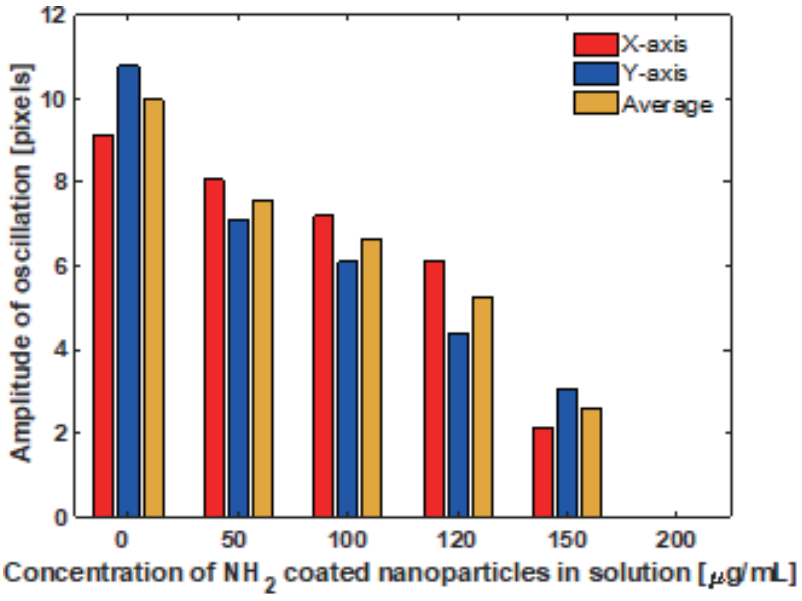

Fig. 9. (Color online) Amplitudes of histogram of oscillation amplitudes along x and y axes for various concentrations of amine-functionalized nanoparticles.

concentration of amine particles. However, the decrease is not uniform. For example, the average oscillation amplitude decreases by about 0.95 μm between 50 and 100 μg/mL, whereas it decreases by 4.07 μm between 100 and 150 μg/mL and the oscillation is nearly 0 (0.005 μm) at a concentration of 200 μg/mL.

4. Discussion and Conclusion

In this work, we proposed a smartphone-based on-chip homogenous medical diagnostics protocol. Our method combined aspects of both homogenous and heterogenous approaches proposed previously to achieve the advantages of portable heterogenous protocols and rapid homogenous protocols. This was achieved by utilizing the well-known fact that the various forces acting on microparticles in a suspension cause them to reach an equilibrium height above a substrate. Thus, horizontal DEP forces were applied by on-chip electrode patterns to enhance the probability of interactions between the particles. The planar arrangement of particles allowed video imaging (2D + time) by a smartphone, as opposed to volumetric observations (3D) obtained in conventional homogenous methods. Particle tracking was performed on high-resolution videos obtained with a smartphone and several signal processing algorithms were used to extract biologically relevant information from raw video observations.

A major feature of our work is that the forces produced by the actuators are DEP in nature and, thus, the magnetic properties of the particles are not used. The relative homogeneity of the DEP forces allows 2D imaging of the particles, which would not be possible under inhomogenous magnetic forces produced by on-chip actuators. We therefore conclude that homogenous sensing can be achieved entirely without the use of magnetism and, thus, magnetic particles are not necessary. Since polystyrene particles have a considerably lower cost than magnetic particles,

we expect our method to have a much lower cost after commercialization than competing magnetic-particle-based approaches in the literature.

Experiments performed on 1-μm-diameter carboxyl-functionalized particles and 200-nm-diameter amine-functionalized particles showed that the oscillation amplitude of the 1-μm-diameter particles decreased as the number of complementary particles was increased. These results serve as the proof of principle of our unique approach to smartphone-based on-chip homogenous sensing with potential applications for biosensing.

We envisage applications of the proposed approach in point-of-care diagnostics, especially in rural locations in developing countries where conventional medical healthcare infrastructure is severely lacking. Going forward, three specific challenges must be addressed to make this approach useful for real-world applications:

(a) The proposed approach must be tested with clinically relevant biomarkers.
(b) The electrical power delivery and optical assembly must be miniaturized to achieve operation in remote locations.
(c) The data processing algorithms must be integrated with cloud computing to allow anyone to upload data onto a cloud server and receive results.

We plan to build upon this work and address all these challenges in the future.

References

1 S. Arumugam, D. A. Colburn, and S. K. Sia: Adv. Mater. Technol. **5** (2020) 1900720. https://doi.org/10.1002/admt.201900720
2 A. C. Sun and D. A. Hall: Electroanalysis **31** (2019) 2. https://doi.org/10.1002/elan.201800474
3 F. A. Cardoso, T. Costa, J. Germano, S. Cardoso, J. Borme, J. Gaspar, J. R. Fernandes, M. S. Piedade, and P. P. Freitas: IEEE Trans. Magn. **48** (2012) 3784. https://doi.org/10.1109/TMAG.2012.2198449
4 S. Cardoso, D. C. Leitao, T. M. Dias, J. Valadeiro, M. D. Silva, A. Chicharo, V. Silverio, J. Gaspar, and P. P. Freitas: J. Phys. D: Appl. Phys. **50** (2017) 213001.
5 S. X. Wang and G. Li: IEEE Trans. Magn. **44** (2008) 1687. https://doi.org/10.1109/TMAG.2008.920962
6 B. Tian, X. Liao, P. Svedlindh, M. Strömberg, and E. Wetterskog: ACS Sens. **3** (2018) 1093. https://doi.org/10.1021/acssensors.8b00048
7 S. Y. Park, H. Handa, and A. Sandhu: Nano Lett. **10** (2010) 446. https://doi.org/10.1021/nl9030488
8 J. A. DuVall, S. T. Cabaniss, M. L. Angotti, J. H. Moore, M. Abhyankar, N. Shukla, D. L. Mills, B. G. Kessel, G. T. Garner, N. S. Swami, and J. P. Landers: Analyst **141** (2016) 5637. https://doi.org/10.1039/C6AN00674D
9 R. Wirix-Speetjens, W. Fyen, K. Xu, J. Boeck De, and G. Borghs: IEEE Trans. Magn. **41** (2005) 4128. https://doi.org/10.1109/TMAG.2005.855345
10 A. D. Henriksen, S. X. Wang, and M. F. Hansen: Sci. Rep. **5** (2015) 12282. https://doi.org/10.1038/srep12282
11 Y. Kumagai, Y. Imai, M. Abe, S. Sakamoto, H. Handa, and A. Sandhu: J. Appl. Phys. **103** (2008) 07A309. https://doi.org/10.1063/1.2833306
12 D. J. Griffiths: Introduction to Electrodynamics (Prentice Hall, New Jersey, 1962).
13 J. D. Jackson: Classical Electrodynamics (John Wiley & Sons, 2007).
14 Q. Cao, X. Han, and L. Li: Lab Chip **14** (2014) 2762. https://doi.org/10.1039/C4LC00367E
15 R. E. Madrid: Electrodes. Handbook of Physics in Medicine and Biology, E. F. Treo, M. C. Herrera, and C. C. Martinez, Eds. (CRC Press Taylor & Francis Group, 2010) pp. 20–21.
16 J. Sharma, S. Ishizawa, R. Yukino, T. Takamura, N. Hanyu, H. Yasuno, H. Handa, and A. Sandhu: Sens. Bio-Sens. Res. **9** (2016) 7. https://doi.org/10.1016/j.sbsr.2016.05.002
17 D. J. Bechstein, J. R. Lee, C. C. Ooi, A. W. Gani, K. Kim, R. J. Wilson, and S. X. Wang: Sci. Rep. **5** (2015) 11693. https://doi.org/10.1038/srep11693
18 Y. Kobori, P. Pfanner, G. S. Prins, and C. Niederberger: Fertility Sterility **106** (2016) 574. https://doi.org/10.1016/j.fertnstert.2016.05.027
19 T. Hergemöller and D. Laumann: The Physics Teacher **55** (2017) 361. https://doi.org/10.1119/1.4999732

20 Y. Rivenson, H. Koydemir Ceylan, H. Wang, Z. Wei, Z. Ren, H. Günaydın, Y. Zhang, Z. Gorocs, K. Liang, D. Tseng, and A. Ozcan: ACS Photonics **5** (2018) 2354. https://doi.org/10.1021/acsphotonics.8b00146
21 D. Quesada-González and A. Merkoçi: Biosens. Bioelectron. **92** (2017) 549. https://doi.org/10.1016/j.bios.2016.10.062
22 J. Sharma, T. Ono, and A. Sandhu: Sens. Bio-Sens. Res. **29** (2020) 100347. https://doi.org/10.1016/j.sbsr.2020.100347
23 Track Master 6000, GitHub Repository: https://www.github.com/dataplayer12/tracking (accessed April 2022).

About the Authors

Jaiyam Sharma received his B.Tech degree from Indian Institute of Technology Delhi in 2014, his master's degree from Toyohashi University of Technology, Japan, and his Ph.D. degree from the University of Electro-Communications, Japan, in 2020. His research interests are in biosensing, especially point-of-care diagnostics. (jaiyamsharma@gmail.com)

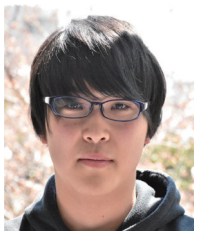

Taisuke Ono received his bachelor's degree from the University of Electro-Communications, Japan, in 2018 and his master's degree from the University of Electro-Communications in 2020. His research interests are in biosensing, especially point-of-care diagnostics. (Taisuke.ono@uec.ac.jp)

Naohito Satake received his bachelor's and master's degrees from the University of Electro-Communications, Japan, in 2019 and 2021, respectively. His research interests are in biosensing and the fabrication of liquid flow cells for wet transmission electron microscopy. (s2033050@uec.ac.jp)

Adarsh Sandhu received his B.Sc. degree from the University of Leeds in 1982 and his Ph.D. degree from the University of Manchester in 1986. From 1986 to 1995, he was a research scientist at Fujitsu Laboratories Ltd.; from 1992 to 1993, he was a visiting scholar at Cavendish Laboratory, Cambridge University; from 1995 to 2002, he worked at the Department of Electrical Engineering, Tokai University; from 2002 to 2010, he was at QNERC, Tokyo Institute of Technology; from 2010 to 2015, he was at EIIRIS, Toyohashi University of Technology. Since 2015, he has been a professor at the University of Electro-Communications, Tokyo. His research interests include 2DEG magnetic biosensors and MEMS for liquid flow TEM. (sandhu@uec.ac.jp)